

## SMECTITE FORMATION IN SUBMARINE HYDROTHERMAL SEDIMENTS: SAMPLES FROM THE *HMS CHALLENGER* EXPEDITION (1872–1876)

JAVIER CUADROS<sup>1,\*</sup>, VESSELIN M. DEKOV<sup>2</sup>, XABIER ARROYO<sup>3,4</sup>, AND FERNANDO NIETO<sup>4</sup>

<sup>1</sup> Department of Mineralogy, Natural History Museum, Cromwell Road, London SW7 5BD, UK

<sup>2</sup> Department of Geology and Paleontology, University of Sofia, 15 Tzar Osvoboditel Blvd., 1000 Sofia, Bulgaria

<sup>3</sup> Departamento de Mineralogía y Petrología, Universidad del País Vasco, 48080 Bilbao, Spain

<sup>4</sup> Departamento de Mineralogía y Petrología and IACT, Universidad de Granada-CSIC, 18002 Granada, Spain

**Abstract**—Clay processes, mineral reactions, and element budgets in oceans continue to be important topics for scientific investigation, particularly with respect to understanding better the roles of chemistry, formation mechanism, and input from hydrothermal fluids, seawater, and non-hydrothermal mineral phases. To that end, the present study was undertaken. Three samples of submarine metalliferous sediments of hydrothermal origin were studied to investigate the formation of smectite, usually Fe-rich, which takes place in such environments. The samples are from the historical collection returned by the British *HMS Challenger* expedition (1872–1876) and kept at the Natural History Museum in London. The samples were collected from the vicinity of the Pacific–Antarctic Ridge and the Chile Ridge. The samples were analyzed by means of X-ray diffraction (XRD), chemical analysis, scanning electron microscopy–energy dispersive X-ray spectroscopy (SEM-EDX), infrared (IR), and transmission electron microscopy–analytical electron microscopy (TEM-AEM). After removal of biogenic calcite the samples appeared to consist mainly of two low-crystallinity phases mixed intimately: Fe/Mn (oxyhydr)oxides and a Si–Al–Mg–Fe phase of similar chemical characteristics to smectite and with variable proportions of the above elements, as indicated by XRD, IR, and SEM-EDX. In particular, analysis by XRD revealed the presence of highly disordered  $\delta$ -MnO<sub>2</sub>. The TEM-AEM analysis showed that Fe/MnOOH particles have Fe/Mn ratios in the range 25–0.2 and textures changing from granular to veil-like as the proportion of Mn increased. The smectite-like material has the morphology and chemistry of smectite, as well as 10–15 Å lattice fringes. Selected area electron diffraction (SAED) patterns indicated a very poorly crystalline material: in some cases distances between diffraction rings corresponded to *d* values of smectite. The smectite composition indicated a main Fe-rich dioctahedral component with a substantial Mg-rich trioctahedral component (total octahedral occupancy between 2.02 and 2.51 atoms per O<sub>10</sub>[OH]<sub>2</sub>). The (proto-) smectite is interpreted to have formed within the metalliferous sediment, as a slow reaction between Fe/MnOOH, seawater (providing Mg), detrital silicates from the continent (providing Si and Al), and X-ray amorphous silica of hydrothermal origin that adsorbed on Fe/MnOOH phases and deposited with them. This material is possibly in the process of maturation into well crystallized smectite.

**Key Words**—*HMS Challenger*, Metalliferous Sediments, Smectite Formation, TEM-AEM.

### INTRODUCTION

*HMS Challenger* traveled around the world between 1872 and 1876 on a scientific expedition with very broad aims. Submarine biological and geological samples were collected throughout the journey. The present study deals with some of the hydrothermal metalliferous sediments that were collected off the coast of Chile between 38–40°S and 98–113°W. Poorly crystallized smectite, frequently Fe-rich, occurs commonly in hydrothermal metalliferous sediments (*e.g.* McMurtry and Yeh, 1981; Cole, 1985; Chamley, 1989; Taitel-Goldman and Singer, 2001). Some of the above studies found that nontronite abundance, in particular, decreased with increasing distance from the hydrothermal site,

indicating a link with the hydrothermal activity. The link could be due to one or more factors such as water temperature, silica concentration, and the presence of Fe<sup>2+</sup>, all of which decrease away from the hydrothermally active site.

The formation of nontronite and Fe-rich montmorillonite in such environments has been interpreted by some authors as a low-temperature reaction between amorphous Fe oxyhydroxide (FeOOH) precipitated from the hydrothermal plume and silica (Chamley, 1989 and references therein). Silica may originate from the dissolution of biogenic siliceous tests, as suggested by their association with smectite (Chamley, 1989 and references therein). In this case, the reacting silica may be dissolved species or biogenic opal contacting FeOOH grains. Cole (1985) found clear signs of dissolution of siliceous debris in association with nontronite in the Bauer Deep (~10°S, 102°W). When observed in more detail, he found that the siliceous tests had nontronite particles attached to them as if growing on their surfaces. Cole (1985) concluded that nontronite formation was mainly the result of the contact

\* E-mail address of corresponding author:

j.cuadros@nhm.ac.uk

DOI: 10.1346/CCMN.2011.0590204

reaction between FeOOH and the siliceous tests, although this reaction would include a silica-dissolution stage. Cole (1985) also considered the possibility that local conditions within the tests would be anoxic and caused Fe reduction, which would facilitate Fe mobilization from FeOOH.

Other authors have suggested a direct precipitation of nontronite from solution, implying the presence of Fe<sup>2+</sup>. Müller and Förstner (1976) envisaged Fe oxidation during hydrothermal fluid discharge, reaction with silica, and nontronite precipitation as occurring approximately simultaneously. Singer *et al.* (1984) suggested a similar scenario. Nontronite precipitated from solution in an active mound because its <sup>87</sup>Sr/<sup>86</sup>Sr signature indicates a large input from seawater, according to Severmann *et al.* (2004).

The temperature of smectite formation derived from O isotope data is a good indicator of proximity to the hydrothermal source and thus of the contribution of the physico-chemical conditions generated by the hydrothermal fluids to the formation of smectite. Cole (1985) obtained an average temperature of 7°C (range 14–4°C) for smectite from the Bauer Deep in the southeast Pacific, which, combined with an estimated error of ±1 to ±7°C, produced a temperature compatible with that of deep ocean waters (3°C). However, McMurtry and Yeh (1981) found a temperature of ~30°C for a single nontronite sample of the same Bauer Deep. Most studies have found smectite-formation temperatures compatible with low-temperature hydrothermal activity. Cole (1983) determined temperatures of 90–140°C and 80°C for nontronite and 160–200°C for montmorillonite-beidelite, each from a different environment in the Atlantis II Deep (Red Sea). Murnane and Clague (1983) found a temperature of 57°C for nontronite from the Juan de Fuca Ridge. Singer *et al.* (1984) obtained a temperature of 26°C for nontronite from the Tahiti–East Pacific Rise–New Zealand transect (which agrees well with the 25°C obtained for coexisting quartz by Stoffers *et al.*, 1984). Köhler *et al.* (1994) obtained 21–67°C for nontronite from the Mariana Trough and 28–44°C for opaline material from the same location, and 52°C for nontronite from the Galapagos Rift. However, Köhler *et al.* (1994) also found features ascribable to bacteria and considered that both the microorganisms and the inorganic chemical conditions may have contributed to nontronite formation. Severmann *et al.* (2004) obtained two ranges of temperature for nontronite formation, one for an active mound of 81–96°C and one for an inactive mound of 54–67°C, both in the Mid-Atlantic Ridge. Dekov *et al.* (2007) determined 30°C for an Al-rich nontronite from the Tyrrhenian Sea. The contribution of hydrothermal fluids in all these cases provides the Si source. Reduced Fe may also have been present in the hydrothermal plume when these nontronites formed and may have played a role in the reaction.

The results above suggest that nontronite and Fe-rich montmorillonite formation is possible in a range of

conditions derived from submarine hydrothermal activity, from relatively close to the point of hydrothermal fluid discharge to locations distant from it or after the activity ceased. The point was illustrated by Heath and Dymond's (1977) investigation of the several sources of sediments in the East Pacific Rise (10–25°S), Bauer Deep, and Central Basin. Those authors concluded that hydrothermal silica was the only silica source for nontronite formation at the Rise, whereas biogenic silica participated increasingly in the reaction toward the basins. The above-mentioned studies indicated, however, that in most cases, the hydrothermal fluids did play a role in the process. Cole (1988) found that smectite composition might be related to the formation conditions, as octahedral Mg and formation temperature were positively correlated in smectite from the Atlantis II Deep. If such were the case for all hydrothermal fields, moving away from the sources of the hydrothermal fluids (higher temperature, possible major involvement of basaltic rock) would give rise to the sequence saponite, Fe-bearing saponite, [perhaps Fe-montmorillonite], Mg-bearing nontronite, and nontronite.

The present study presents a macroscopic and microscopic analysis of non-crystalline material of smectitic composition associated with FeOOH from the metalliferous sediments collected in the HMS Challenger expedition, in order to investigate its possible link to smectite genesis. The study was intended to further understanding of smectite genesis in these environments and, in particular, to investigate mineral phases that appear to represent smectite in its formation stage. The study completes a more general one by Dekov *et al.* (2010) of sediments from an area that has been scarcely sampled, and thus also has the effect of completing available information about metalliferous sediments in this part of the South Pacific.

## MATERIALS AND METHODS

Three samples were selected for this study (labeled 292, 293, and 294) from a set of eight. The selection criteria were the dominance of the metalliferous sediment component and minimum detrital continental contribution. The samples were collected from the junction of the Pacific, Antarctic, and Nazca plates (Figure 1). Magmatic activity in the area is significant and causes intense hydrothermal activity which has resulted in this very large metalliferous sediment field. The southern part of the field was delineated after several expeditions in the 1960–70s (Boström, 1973; Gurvich, 2006). Two hydrothermal fields that contribute to the southern extent of this metalliferous field have been found (black and gray squares, Figure 1) on the Pacific–Antarctic Ridge (Stoffers *et al.*, 2002) and on the Chile Ridge (Marienfeld and Marchig, 1992). The regional pattern of abyssal circulation (in a northeasterly direction; Lonsdale, 1976) partly controls the dispersal

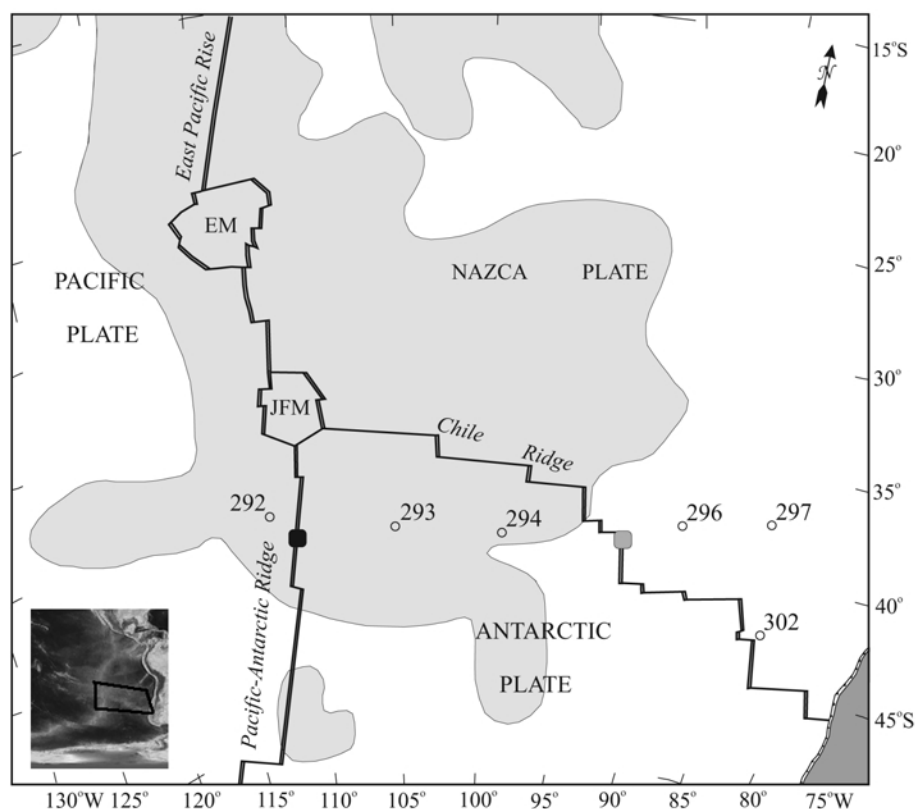


Figure 1. Map indicating where samples 292, 293, and 294 were collected (other sites not included in the present study). The squares, black on the Pacific–Antarctic Ridge and gray on the Chile Ridge, are the locations of two observed hydrothermal fields. The extent of the area covered with metalliferous sediments is marked in gray. EM: Easter microplate; JFM: Juan Fernandez microplate. The inset indicates the approximate area covered by the detailed map.

of the hydrothermal plume fallout and the distribution of distal metalliferous sediments.

After the post-cruise on-shore investigation (Murray and Renard, 1891), the sediments were donated to the Natural History Museum, London, where they were kept sealed in the original glass jars and tubes. A complete description of the specimens, as found in the collection, was provided by Dekov *et al.* (2010). Aliquots from the samples were finely ground in an agate mortar. Their bulk mineralogy was studied by analyzing sedimented powder mounts in a position-sensitive detector X-ray diffractometer (Enraf-Nonius Powder Diffraction System 120) using monochromatic  $\text{CuK}\alpha$  radiation, at 40 kV and 35 mA, from 2 to  $120^\circ 2\theta$ . This type of apparatus collects the diffracted radiation throughout the entire angular range simultaneously, using an arch-shaped detector. The angle between the incident beam and the sample plane was  $2\text{--}3^\circ$ . The samples were spun to maximize the analyzed volume and the counting time was 15 min. For calibration, Si,  $\text{Y}_2\text{O}_3$ , and Ag behenate standards were used. This analysis (not shown) indicated that samples 292 and 293 were dominated by calcite (of biological origin, as shown by SEM analyses). The chemical composition of the major elements was

measured using inductively coupled plasma-atomic emission spectroscopy (ICP-AES) (Varian VISTA PRO). The total dissolution of the bulk sample was performed by  $\text{HF-HClO}_4$ -aqua regia attack in closed bottles in a microwave oven (Thompson and Walsh, 2003). The accuracy of the results was controlled with international standards and yielded errors of  $\pm 0.2\text{--}2.5\%$  of the measured values. Water content in the samples was measured by means of C-H-N elemental analysis using a CE Elantech Flash 1112 EA Soil Analyzer. Samples were heated at  $900^\circ\text{C}$  and the resulting  $\text{H}_2\text{O}$  vapor quantified. Blanks and aspartic acid standard were also analyzed. The analytical error was less than  $\pm 4.5\text{ wt.}\%$  of  $\text{H}_2\text{O}$ . Observations by SEM were made on C-coated fragments of bulk samples both as chips and loose sediment glued to carbon stubs. They were imaged with secondary and back-scattered electrons and analyzed chemically by means of EDX, using a JEOL 5900LV and a Leo 1455VP electron microscopes both equipped with an Oxford Instruments INCA EDX detector. Chemical analyses were calibrated using mineral standards.

Samples 292 and 293 were treated to remove calcite using 2% acetic acid in water with constant stirring and

ultrasonic treatment to disaggregate particles, then centrifuged at 18,000 g in an Eppendorf 5810R centrifuge. The process was repeated three times and finally the solid was washed four times with distilled water by centrifugation. The calcite-free fraction was analyzed as air-dry oriented mounts to emphasize clay-mineral peaks. The calcite-free samples were analyzed using a Philips PW 1050 diffractometer with CuK $\alpha$  radiation, equipped with a graphite monochromator, at 42 kV and 42 mA, in the range 2–40°2 $\theta$ , at 0.02°2 $\theta$  steps and 10 s per step. Infrared analysis was carried out using a Perkin Elmer Spectrum One spectrometer. Samples were prepared as pellets with KBr (~1 mg clay:200 mg KBr) and analyzed in transmission mode in the range 4000–200 cm<sup>-1</sup>, with a resolution of 4 cm<sup>-1</sup> and accumulating 10 scans per analysis. The samples were also analyzed using TEM with analytical electron microscopy (AEM) in STEM mode. The microscope was a Philips CM20 (STEM, at the C.I.C., University of Granada), with an EDAX solid-state EDX detector, operating at 200 kV. Analyses were obtained from powdered portions dispersed in alcohol and deposited on a holey C-coated Au grid. This mode of preparation disperses individual grains of minerals onto the grid surface. Albite, biotite, spessartine, muscovite, olivine, and titanite standards were used to obtain K-factors for the transformation of intensity ratios to concentration ratios following Cliff and Lorimer (1975).

## RESULTS

### XRD

The XRD analysis of oriented mounts showed that they consisted mainly of poorly crystallized material, with small amounts of crystalline phases of hydrothermal or related origin (barite, possibly natrojarosite and mackinawite) and of continental detrital origin (plagioclase, mica, kaolinite, quartz, and possibly K-feldspar; Figure 2, Table 1). The proportion of detrital minerals increased from sample 292 to 294, in good agreement with their relative proximity to the continent (Figure 1). Peak 1, in the low-angle region of the XRD patterns of the three samples, is broad and has low intensity, which suggests a trace amount of smectite or smectite which is poorly crystallized. Smectite is also suggested by the broad shoulder at ~35°2 $\theta$  in samples 292 and 294 (not marked in Figure 2) and the sharper peak in the same position in sample 293 (peak 14). The wide peak at ~20°2 $\theta$  (4.45–4.50 Å) suggests poorly crystalline phyllosilicates. Such assignment is supported by reports of the initial stages of 2:1 and 1:1 phyllosilicate crystallization indicating that the ~4.5 Å structural repeat develops early and clearly in a variety of physicochemical settings (Tazaki *et al.*, 1989; Mazer *et al.*, 1992; Huertas *et al.*, 2000, 2004). The broad, intense peak at ~4.20 Å may correspond to goethite of very low crystallinity. Other peaks of lower intensity and of

sharper appearance also indicate goethite (Table 1). Poorly crystallized goethite is a very likely phase given the nature of the samples. X-ray amorphous silica and/or an amorphous silicate phase may also contribute intensity to the broad peaks at 19–23°2 $\theta$ . The amorphous silica band in this area is much broader, however, and is typically centered at 23°2 $\theta$ , spanning 15–40°2 $\theta$ ; thus, its contribution in the present samples should be small.

The peak at ~2.45 Å is intense and broad, suggesting an abundant and poorly crystallized phase. Goethite is a possible contributor to this peak but its relative intensity and that at ~4.20 Å indicate that some other phase should be contributing intensity to the 2.45 Å peak. This phase is probably  $\delta$ -MnO<sub>2</sub>, a material related to birnessite, which often shows only two broad peaks, at 2.45 and 1.40 Å, and is common in marine Fe-Mn nodules (Brown, 1980). The powder XRD analysis of the

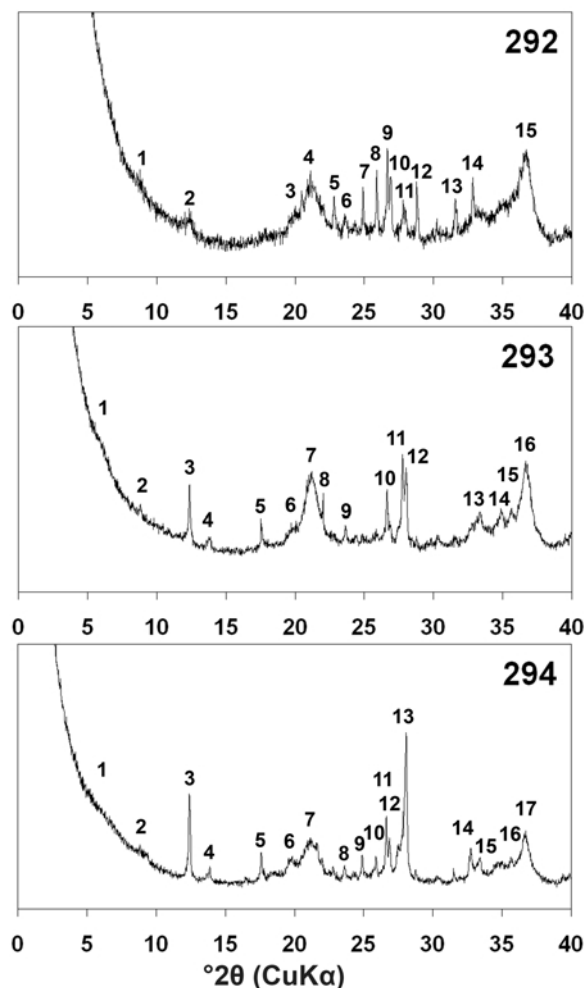


Figure 2. XRD traces of the oriented, air-dried mounts of the metalliferous sediments after calcite dissolution. The numbers are peak labels and their corresponding phases are provided in Table 1.

Table 1. XRD peaks from Figure 2 and their assignment.

Sample 292			Sample 293			Sample 294		
Peak	<i>d</i> value (Å)	Mineral	Peak	<i>d</i> value (Å)	Mineral	Peak	<i>d</i> value (Å)	Mineral
1	10.0	Dehydrated smectite?/ mica?	1	15	Smectite	1	~15	Smectite
2	7.1	δ-MnO <sub>2</sub> ?/kaolinite?	2	10.0	Mica	2	10.0	Mica
			3	7.15	Kaolinite	3	7.13	Kaolinite
			4	6.41	Plagioclase	4	6.37	Plagioclase
			5	5.04	Mica/natrojarosite?/ mackinawite?	5	5.04	Mica/natrojarosite?/ mackinawite?
3	4.45	Phyllosilicates?/barite	6	4.47	Phyllosilicates?	6	4.50	Phyllosilicates?
4	4.20	Goethite?/low-crystallinity silicate?	7	4.20	Goethite?/ low-crystallinity silicate?	7	4.20	Goethite?/ low-crystallinity silicate?
			8	4.03	Plagioclase			
5	3.89	Barite, plagioclase				8	3.76	Plagioclase
6	3.76	Plagioclase	9	3.77	Plagioclase	9	3.58	Kaolinite
7	3.58	Kaolinite, barite				10	3.44	Barite
8	3.44	Barite, plagioclase				11	3.34	Quartz
9	3.34	Quartz	10	3.34	Quartz	12	3.317	K-feldspar, barite
10	3.315	K-feldspar, barite						
11	3.209, 3.192	Plagioclase	11	3.212	Plagioclase			
			12	3.184	Plagioclase	13	3.179	Plagioclase
12	3.097	Barite						
13	2.834	Barite, plagioclase	13	2.686	Goethite	14	2.732	Barite
14	2.725	Barite	14	2.569	Smectite?	15	2.683	Goethite
			15	2.517	Goethite	16	2.517	Goethite
15	2.448	δ-MnO <sub>2</sub> /goethite?	16	2.451	δ-MnO <sub>2</sub> /goethite?	17	2.448	δ-MnO <sub>2</sub> /goethite?

bulk sample not dominated by calcite (not shown) indicated the presence of a small, wide feature at ~1.40 Å, which may correspond to the δ-MnO<sub>2</sub> phase. The intensity of the 2.45 Å peak may be enhanced by the contribution of goethite and thus become more prominent. Birnessite has a peak at 7.1–7.13 Å, and it may contribute to the peak in this position in all three samples, although kaolinite is evidently present in samples 293 and 294. Turbostratic birnessite typically has very low intensity or no 001 peak series, where the 7.1–7.13 Å peak corresponds to the 001 reflection, and the only readily observable peaks are those at ~2.4 and ~1.4 Å (Jürgensen *et al.*, 2004). Heath and Dymond (1977) also assigned the 2.45 Å peak, found in patterns of metalliferous sediments from the East Pacific Rise area, to δ-MnO<sub>2</sub>. From the XRD evidence, from previous assignments made, and given the nature of our samples (submarine metalliferous sediments rich in Fe and Mn), the intense peak at 2.45 Å probably corresponds mainly (with a possible contribution by goethite) to the δ-MnO<sub>2</sub> phase.

#### Bulk chemistry

The bulk chemical analyses of the metalliferous sediments showed that samples 292 and 293 contained a large amount of calcite (bottom CaO values in Table 2),

which was shown by SEM to be of biogenic origin (see below). As no calcite XRD peaks were observed in sample 294 (Figure 2), its Ca content was assigned to plagioclase. The small differences in the relative

Table 2. Chemical composition (wt.%) of the three samples of metalliferous sediments after subtraction of calcite.

Samples:	292	293	294
CaO	2 <sup>†</sup>	2 <sup>†</sup>	2.25 <sup>‡</sup>
Al <sub>2</sub> O <sub>3</sub>	2.54	4.94	7.35
Fe <sub>2</sub> O <sub>3</sub>	32.96	34.69	26.89
K <sub>2</sub> O	0.33	0.62	1.43
MgO	3.61	2.20	2.59
MnO	11.76	9.93	6.43
Na <sub>2</sub> O	2.00	0.64	1.16
P <sub>2</sub> O <sub>5</sub>	1.62	1.38	1.09
SiO <sub>2</sub>	13.63	15.76	26.29
TiO <sub>2</sub>	0.22	0.45	0.42
H <sub>2</sub> O	27.03	28.07	24.80
Total	97.70	100.67	98.71
CaO*	53.34	30.51	2.25

<sup>†</sup> Estimated.

<sup>‡</sup> No calcite present in the bulk sediment.

\* Values correspond to the bulk sediment before subtraction of calcite.



intensities of the plagioclase peaks in the three samples (Figure 2) indicate very similar plagioclase content and, thus, the 2% CaO estimated in samples 292 and 293 was attributed to plagioclase rather than to calcite. The calcite contribution to CaO was then subtracted from the analyses of samples 292 and 293 and renormalized (Table 2). The phosphorous content is relatively large in terms of that found for metalliferous sediments (Froelich *et al.*, 1977; McMurtry and Yeh, 1981; Severman *et al.*, 2004). No apatite or other P crystalline phase was found using XRD and so P may be in the form of non-crystalline organic matter or adsorbed onto the Fe/MnOOH phases (Froelich *et al.*, 1977). As only a small amount of organic matter is present (see below) and Froelich *et al.* (1977) found that hydrothermal FeOOH is an effective scavenger of P from seawater, adsorption onto Fe/MnOOH phases is the most likely possibility. The calcite-free composition is rich in Fe and has significant Mn, as expected in metalliferous sediments of hydrothermal origin. The water content is large and probably present in Fe/Mn oxyhydroxides, clays, and amorphous silica. The silica content is also large and the Al and Mg contents are significant, *i.e.* in concentrations greater than the crystalline aluminosilicate phases present would suggest.

#### SEM-EDX

Examination by SEM showed the abundant biogenic calcite in samples 292 and 293 to consist of tests of *Globigerina bulloides*. The majority of the non-biogenic material consisted of aggregates of very small particles of irregular shape (Figure 3). The chemical composition of these grains varied from Fe-Mn almost exclusively to Si-Al-Mg-Fe with various relative proportions of these elements. The first group was infrequent and obviously corresponded to Fe/Mn oxyhydroxides. The second group was abundant, usually containing Mn also (Figure 3). Given the large Fe and Mn contents in the samples, much of the Fe/Mn oxyhydroxides present must be mixed intimately with the silicate phases, so that both types of grains were analyzed together by EDX. Iron and Mn mapping of the samples was carried out using EDX (not shown) and both elements appeared to be uniformly distributed, although Mn tended to segregate more. Such uniform distribution confirms that Fe/Mn-OOH is mixed intimately with the other components of the sediments. Sodium and Cl appear frequently and correspond to sea salt.

The Si-Al-Mg composition of the silicate phases suggests smectitic phases (Figure 3). The Si-Al-Mg particles are ubiquitous in the samples, even though XRD revealed that smectite peaks have very low intensity. A poorly ordered phase with composition approaching that of smectite, both tri- and dioctahedral (Figure 3), is indicated. The EDX analyses cannot indicate whether some of the Fe and Mn is partly in the silicate phase. Occasionally, grains of other minerals were observed,

including all those that appeared in the XRD patterns. The most frequent were plagioclase crystals (not shown) of large size and well developed faces, sometimes with signs of dissolution. A few grains consisting exclusively of Si were found (Figure 3d). They had signs of dissolution and could be either quartz or amorphous silica grains.

#### IR

The IR spectra revealed broad features in the three samples after removal of calcite, including intense and broad O—H stretching bands, indicating low crystallinity and large water content (Figure 4). The band assignments have been well established and reported by Russell and Fraser (1994). The large band at  $\sim 3400\text{ cm}^{-1}$  is due to O—H stretching of adsorbed water or hydroxyls in a material of low crystallinity. This band is compatible with ferrihydrite or some form of poorly crystallized FeOOH and silicate. These phases can contain molecular water and OH groups, consistent with the observed bands. The smaller band at  $1630\text{ cm}^{-1}$  and the shoulder at  $1545\text{ cm}^{-1}$  correspond to O—H bending of molecular water. The plateau centered at  $\sim 1425\text{ cm}^{-1}$  in sample 292 probably corresponds to organic matter, as do the several sharp bands at  $2960\text{--}2850\text{ cm}^{-1}$ . The low intensity of these organic-related bands indicates a minor organic component. The large bands with maxima at  $1030$  and  $470\text{ cm}^{-1}$ , corresponding to the Si—O stretching system and several lattice vibrations, respectively, are compatible with a silicate phase. The shoulder at  $915\text{ cm}^{-1}$  is typically assigned to the AlAl—O—H bending mode in the octahedral sheet of phyllosilicates. Sample 294 displayed a clear shoulder at  $875\text{ cm}^{-1}$ , corresponding to AlFe—O—H bending in phyllosilicates. This band appears in that position in samples with a significant proportion of octahedral Fe. The small shoulder at  $\sim 818\text{ cm}^{-1}$  in sample 294 is consistent with an FeFe—O—H bending mode. Thus, sample 294 apparently contains more Fe in the poorly crystallized phyllosilicate phase than the other samples.

The band at  $800\text{ cm}^{-1}$  (along with a small shoulder at  $780\text{ cm}^{-1}$ ) probably corresponds to quartz. Other less crystalline forms of silica also have a relatively sharp band at  $\sim 950\text{ cm}^{-1}$ . The shoulder at  $670\text{ cm}^{-1}$  is compatible with the O—H bending band in Mg-rich trioctahedral environments, which appears in the region  $650\text{--}670\text{ cm}^{-1}$ . This band is near  $650\text{ cm}^{-1}$  in smectite and near  $670\text{ cm}^{-1}$  in talc, which would suggest traces of talc or talc-like material in the samples. However, the location of the band may be affected by the low crystallinity of the phyllosilicate phases and IR spectroscopy alone cannot indicate the exact nature of the phase giving rise to this band.

#### TEM-AEM

The samples analyzed appeared, under TEM inspection, as a mixture of particles with variable morphology,

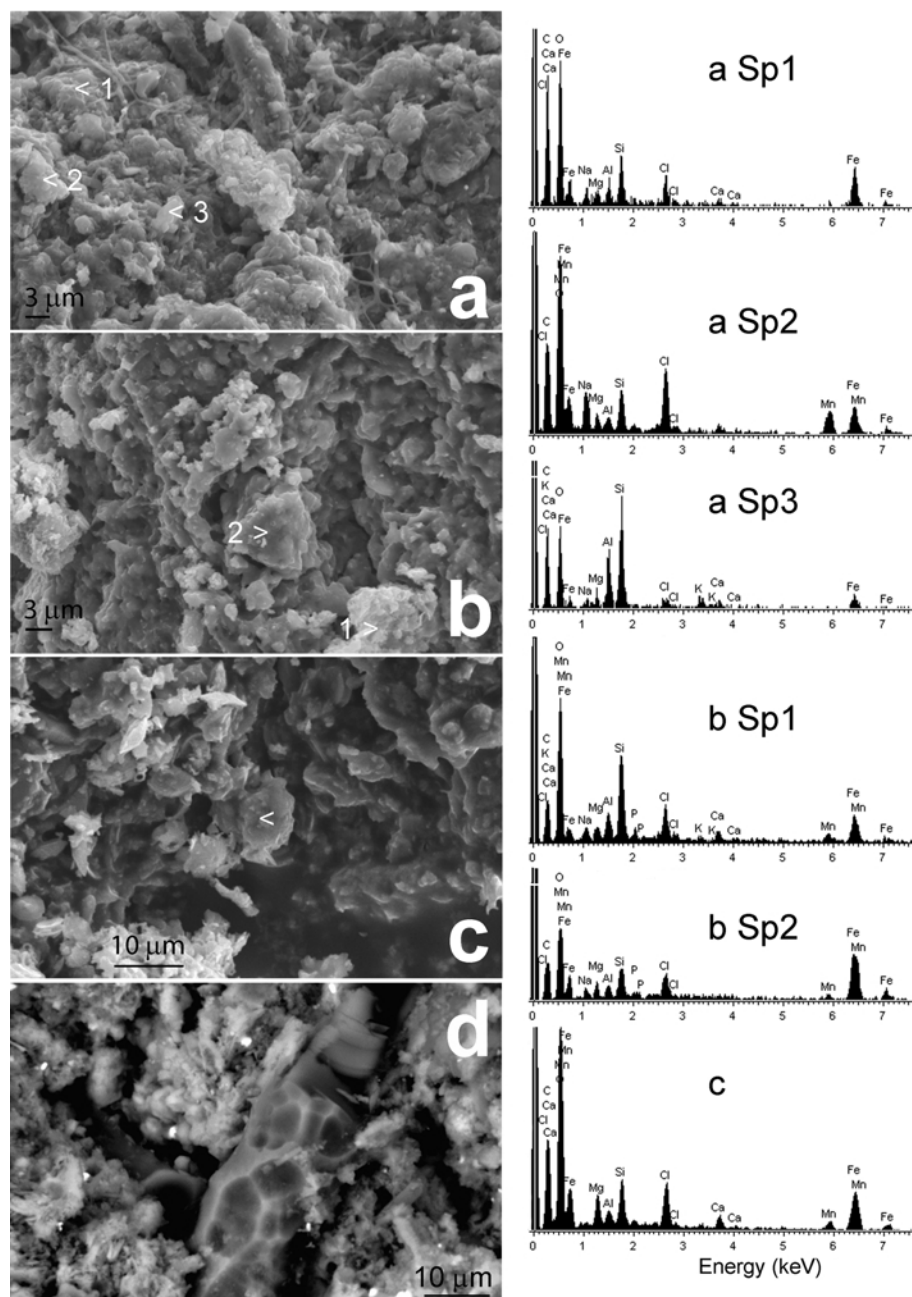


Figure 3. SEM images of the metalliferous sediments and EDX spectra of selected areas. The spots analyzed are marked on the photographs and the spectra are labeled to indicate the photograph and spot to which they correspond. (a), (b), and (c) are secondary electron images and show fine-grained material, probably a mixture of Fe/Mn oxyhydroxides and a gel silicate phase of variable composition. The fluid-like material at the lower right side of (c) is NaCl from seawater. (d) Back-scattered electron image showing a corroded grain of some silica phase. The bright spots in (d) are metal-rich and water-poor in composition.

suggestive of the several phases that were found in the XRD analysis. Analysis by AEM of individual grains confirmed the nature of such phases. The attention was focused on smectite and its relationship to Fe/MnOOH phases. Iron and Mn oxyhydroxides always contained small amounts of Si, Al, and Mg (Figure 5). Their

morphology varied depending on their Fe/Mn ratio. Iron-rich particles were in the majority and exhibited a granular texture (Figure 5a) which changed to a veil-like texture as the proportion of Mn increased (subtle change in morphology in the area marked by the lower arrow in Figure 5a; veil-like morphology in Figure 5b).

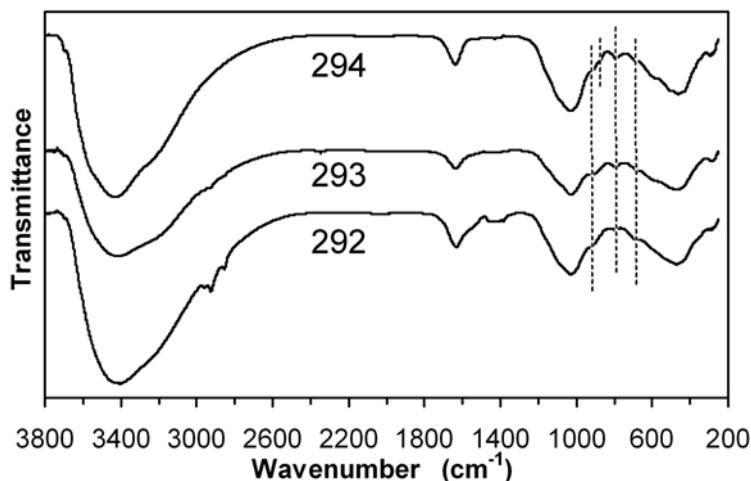


Figure 4. IR spectra of the three metalliferous sediments after calcite dissolution. The dashed vertical lines correspond to the frequency values 915, 875 (observed clearly in sample 294 only), 800, and 670  $\text{cm}^{-1}$ . See text for their assignment.

Manganese-rich particles had an appearance very similar to the veil-like smectitic texture.

In intimate mixture with the Fe/MnOOH phases were abundant smectite-like particles, according to their

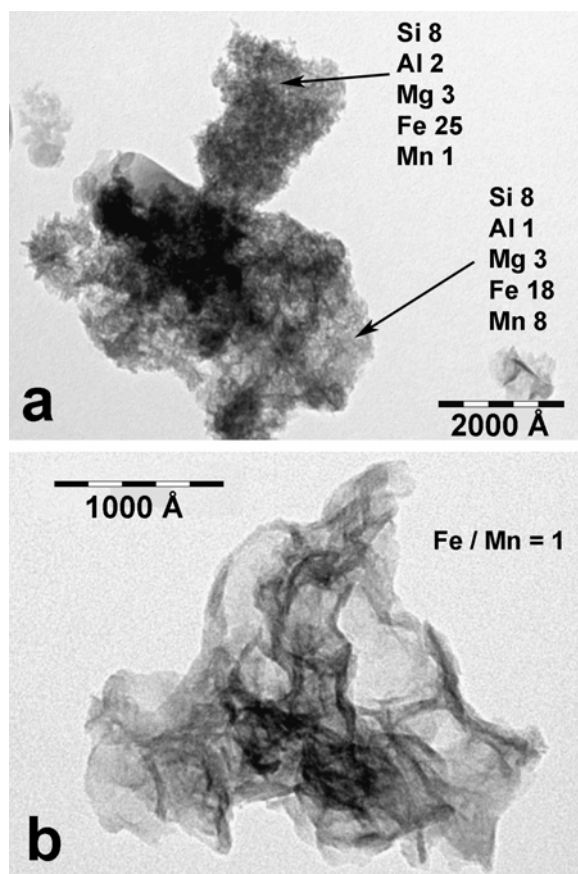


Figure 5. TEM images and chemical data for Fe/MnOOH particles with different Fe/Mn ratios. The texture of the particles changes from granular to veil-like with increasing Mn content.

morphology and chemical composition (similar to those found with SEM-EDX, Figure 3). The smectite-like morphology typically consisted of extended flat particles or groups of particles a few thousands of Å across (Figure 6a,d). In some cases, the particles consisted of an accumulation of laths in random orientation (Figure 6b). In other cases, packets of layers lay with their  $c^*$  axis perpendicular to the electron beam and fringe images were observed, with the typical wavy appearance of smectite (with numerous defects, such as layer merging) and fringe width of 10–15 Å, also typical of smectite under TEM conditions (Figure 6c). Selected area electron diffraction patterns were obtained from many of the smectite-like particles to investigate their crystallinity. Analytical electron microscopy data were also obtained from the same particles. After analysis of the AEM data (see below), the SAED patterns of those particles that could be identified as smectite were selected and studied (Table 3). Most indicated low crystallinity, with poorly defined  $hk$  ring patterns, which may justify labeling these particles as proto-smectite.

The AEM analyses of the Fe/MnOOH and smectite-like particles (Table 4, Figure 7) showed a large variability in composition from relatively rich in Si, usually corresponding to smectite or proto-smectite particles, to Fe/Mn-rich with low Si. However, as indicated above, no particles consisting of Fe- or Mn-oxyhydroxide only were found; Si, Al, and Mg were always present, probably indicating mixture with smectite or proto-smectite. One single analysis, apparently covering two particles of different nature, produced a large Si excess over all others (Figure 7). The SAED of the two combined particles produced strong diffraction with multiple orientation characteristics of a phase that could not be recognized, but was suspected to be quartz. Considering the possible presence of dioctahedral and trioctahedral smectite, the particles likely to be smectite



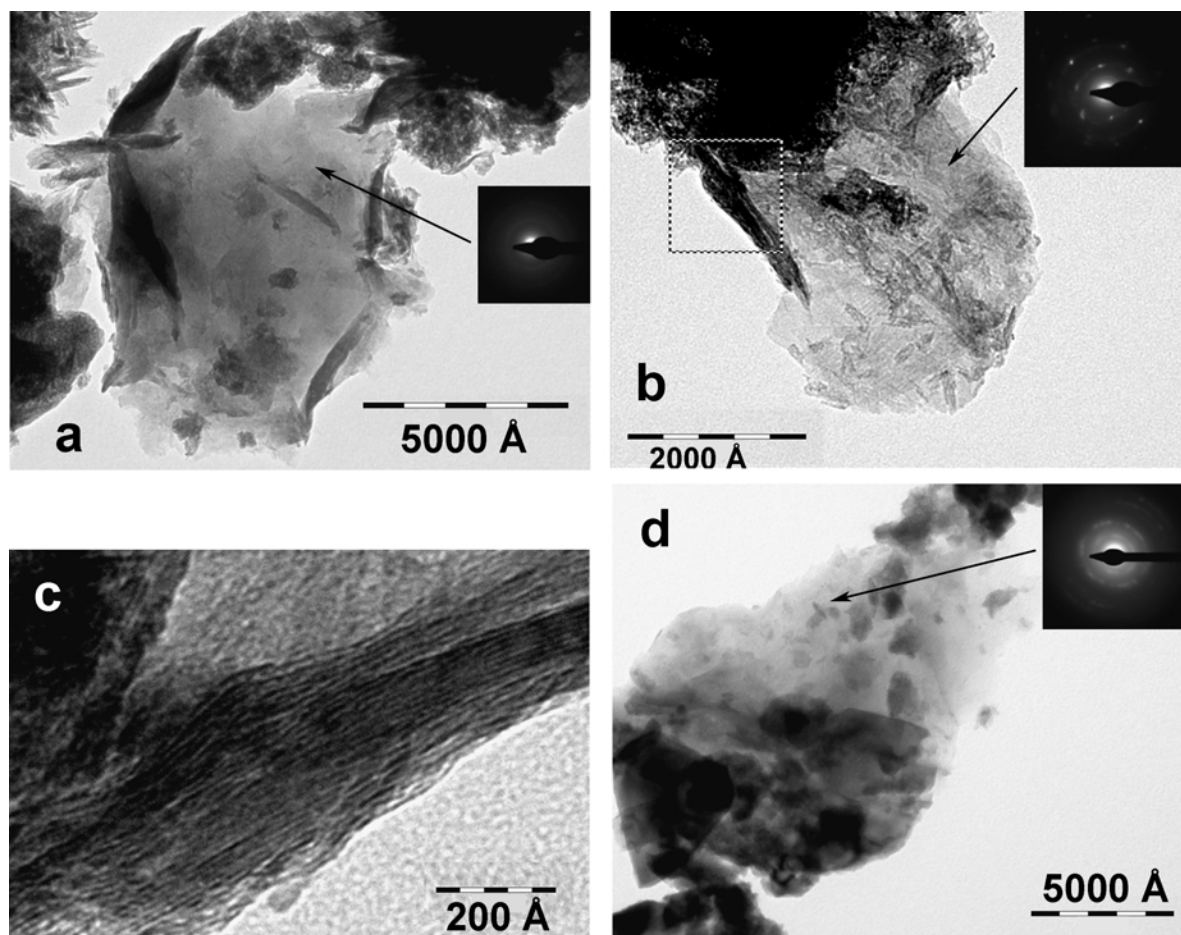


Figure 6. TEM images and SAED patterns of smectite particles with different octahedral compositions (see Table 5): (a) sample 294, analysis 1-S2; (b) sample 293, analysis 11-J; (c) lattice-fringe image of the area marked in (b), after a  $\sim 90^\circ$  counter-clockwise rotation; (d) sample 293, analysis 2-S.

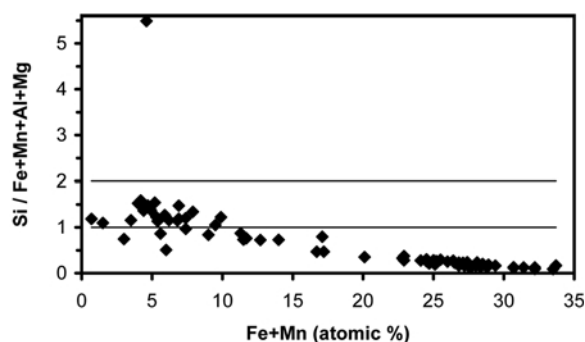


Figure 7. Atomic ratio (Si/octahedral cations) vs. the sum of Fe and Mn atoms, both from AEM analysis. The cationic ratio (vertical axis) provides the approximate range (between 1 and 2, see text) where smectite particles (both di- and trioctahedral) should plot. The other particles are a mixture of Fe/MnOOH and smectite or proto-smectite, where the oxyhydroxide component increases to the right. The analysis with the large Si content is suspected to have included quartz.

were those for which  $1 \leq \text{Si}/(\text{Al}+\text{Fe}+\text{Mg}+\text{Mn}) \leq 2$ , where the minimum ratio corresponds to a trioctahedral smectite (octahedral occupancy assumed to be 3) with a small assumed Si content of 3 in the structural formula; and the maximum ratio corresponds to a dioctahedral smectite (octahedral occupancy 2) with Si content of 4. The structural formulae for these analyses and for two others with  $\text{Si}/(\text{Al}+\text{Fe}+\text{Mg}+\text{Mn})$  of 0.97 and 0.86 were calculated and produced good matches (Table 5), as indicated by the balance in electrostatic charge between the negative lattice and the positive interlayer cations. In all cases, the morphology was compatible with smectite rather than any other phyllosilicate, given the thinness and irregularity of the particles.

Analysis 19-J of sample 292 (Table 5) appears to correspond to Fe-talc. This is a very large particle with straight edges which are perpendicular to each other, and very sharp and regular SAED dot diffraction patterns. Iron occupies some of the tetrahedral sites and Mg is in excess of 3 in the octahedral sheet. Such characteristics

Table 3. Description of the morphology (TEM) and electron-diffraction-pattern characteristics (SAED) of the smectite particles that were identified using AEM. The corresponding AEM analysis label and mineralogy description (from Table 5 below) are provided for reference.

Sample	AEM		SAED characteristics	TEM characteristics
292	1-S	Nontronite	Weak, broad rings	Indistinct, flat
293	4-J	Fe-Mont	Sharp dot pattern	Indistinct flat particle; regularly shaped particles on it
293	7-J	Nontronite	Very weak, broad rings and weak dot pattern (from Fe/MnOOH?)	Veil morphology and Mn-rich Fe/MnOOH grain
293	10-J	Fe-Mont	Weak, broad rings	Veil morphology; some lattice fringes
293	11-J	Nont (Mn)	Very weak dot pattern and rings; only 2–3 rings	Lattice fringes
293	12-J	Fe-Mont	Very weak dot pattern and rings; only 2–3 rings	Laths
293	16-J	Nontronite	Very weak, discontinuous rings	Long laths; some lattice fringes
293	20-J	Nontronite	Very weak, discontinuous, deformed rings	Long lenticular particles (some with lattice fringes) and large, flat area
293	21-J	Nontronite	Very weak, diffuse rings	Veil morphology; some lattice fringes
293	23-J	Fe-Al-Mg	Very diffuse, deformed rings	Indistinct, flat
293	2-S	Nont-Sap	Very diffuse, discontinuous, deformed rings	Indistinct, flat, with some irregular particles
294	2-S1	Nontronite	Diffuse rings	Indistinct, flat, with some irregular particles
294	3-S1	Nont (Mn)	Weak, diffuse, deformed rings with deformed, weak dot pattern (both smectite?)	Indistinct, veil morphology
294	7-S1	Nont-Sap	No SAED available	Indistinct, flat; some irregular particles
294	8-S1	Nont-Sap	No SAED available	Indistinct; some irregular particles; 2–3 wavy lattice fringes
294	9-S1	Nont-Sap	Weak, diffuse, discontinuous, deformed rings	Indistinct, flat
294	10-S1	Nont-Sap	No SAED available	Indistinct; some irregular particles
294	12-S1	Fe-Al-Mg	Intense but diffuse, discontinuous rings	Flat; some irregular particles on it
294	14-S1	Nontronite	Weak, diffuse rings	Indistinct
294	19-S1	Mg-Fe-Al	Very diffuse, deformed rings	Indistinct; a few lattice fringes
294	21-S1	Nontronite	Weak, diffuse rings	Indistinct; laths
294	1-S2	Fe-Mont	Diffuse circle with two weak rings	Indistinct, flat; some irregular particles

have been reported previously for talc (Newman and Brown, 1987). Analysis 15-S1 from sample 294 corresponds to mica, as indicated also by a well defined SAED pattern in this area (not shown). Analysis 12-S1, also in sample 294, displays a high interlayer charge of 0.75 but the SAED pattern in this area is more typical of

smectite, with diffraction rings the definition of which varies from point to point. All other analyses suggest smectite. The analysis of the octahedral composition of these clays reveals important features regarding their nature. Most of the values correspond to a dominantly dioctahedral phase (Figure 8), with octahedral Al + Fe

Table 4. Chemical analysis (AEM) of a selection of Fe/MnOOH grains showing their compositional range.

Sample	Analysis	Si	Al	Mg	Fe	Mn	Ti	K	Ca	Na
292	12-J	5.6	1.4	3.8	16.4	13.0	0.0	0.0	2.5	0.0
292	13-J	3.5	1.0	5.8	10.0	23.5	0.0	0.0	1.8	0.0
292	15-J	7.8	1.9	3.0	25.1	0.9	0.0	0.0	0.8	0.0
292	16-J	8.2	0.7	3.1	18.2	8.2	0.0	0.2	2.6	0.0

Table 5. Structural formulae of the phyllosilicate particles analysed using AEM.

Sample	Analysis	Si	Tet Al	Tet Fe	Oct Al	Mg	Fe	Mn	Ti	Sum Oct	K	Ca	Na	Int ch
292	19-J	3.85	0.00	0.13	0.00	3.12	0.00	0.00	0.00	3.12	0.00	0.00	0.00	0.00
292	1-S	3.27	0.73	0.00	0.03	0.69	1.67	0.00	0.00	2.39	0.14	0.05	0.00	0.25
293	4-J	3.35	0.65	0.00	1.29	0.35	0.59	0.02	0.00	2.25	0.16	0.05	0.00	0.26
293	7-J	3.33	0.67	0.00	0.91	0.23	1.06	0.02	0.00	2.22	0.19	0.03	0.00	0.26
293	10-J	3.60	0.40	0.00	0.97	0.40	0.81	0.03	0.00	2.21	0.09	0.05	0.00	0.19
293	11-J	3.14	0.86	0.00	0.68	0.41	1.06	0.25	0.00	2.39	0.18	0.09	0.00	0.35
293	12-J	3.72	0.28	0.00	1.10	0.24	0.71	0.02	0.00	2.07	0.26	0.03	0.00	0.33
293	16-J	3.45	0.52	0.03	0.00	0.58	1.61	0.09	0.00	2.28	0.00	0.19	0.00	0.38
293	20-J	3.48	0.52	0.00	0.67	0.53	1.00	0.04	0.00	2.23	0.21	0.09	0.00	0.39
293	21-J	3.69	0.31	0.00	0.47	0.52	1.15	0.05	0.00	2.20	0.16	0.07	0.00	0.30
293	23-J	3.69	0.31	0.00	0.74	0.63	0.79	0.04	0.00	2.20	0.25	0.07	0.00	0.39
293	2-S	3.46	0.54	0.00	0.27	1.28	0.96	0.00	0.00	2.51	0.09	0.11	0.00	0.30
294	2-S1	3.36	0.64	0.00	0.40	0.46	1.30	0.00	0.00	2.16	0.25	0.18	0.00	0.60
294	3-S1	3.35	0.65	0.00	0.53	0.42	1.11	0.11	0.00	2.17	0.23	0.21	0.00	0.65
294	7-S1	3.56	0.44	0.00	0.17	1.35	0.94	0.00	0.00	2.47	0.18	0.04	0.14	0.39
294	8-S1	3.82	0.18	0.00	0.34	1.04	0.91	0.00	0.00	2.30	0.11	0.07	0.09	0.33
294	9-S1	3.72	0.28	0.00	0.43	0.99	0.79	0.00	0.02	2.23	0.10	0.19	0.09	0.58
294	10-S1	3.67	0.33	0.00	0.31	1.26	0.78	0.00	0.00	2.35	0.11	0.12	0.18	0.53
294	12-S1	3.58	0.42	0.00	0.66	0.59	0.83	0.00	0.00	2.09	0.21	0.09	0.37	0.75
294	14-S1	3.50	0.50	0.00	0.34	0.40	1.34	0.03	0.03	2.15	0.07	0.10	0.16	0.44
294	15-S1	3.15	0.85	0.00	1.53	0.23	0.26	0.00	0.00	2.02	0.76	0.00	0.25	1.00
294	19-S1	3.01	0.99	0.00	0.51	1.00	0.96	0.04	0.00	2.51	0.14	0.12	0.11	0.50
294	21-S1	3.30	0.70	0.00	0.57	0.41	1.15	0.05	0.00	2.18	0.21	0.11	0.19	0.62
294	1-S2	3.68	0.32	0.00	1.15	0.26	0.69	0.00	0.00	2.10	0.07	0.10	0.00	0.28

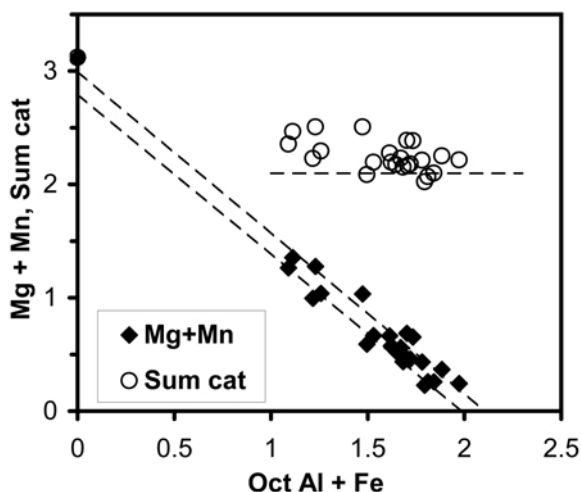


Figure 8. Octahedral Al + Fe vs. octahedral Mg + Mn and the sum of all octahedral cations from phyllosilicate particles. Values correspond to the structural formulae per  $\text{O}_{10}(\text{OH})_2$ . Analyses with  $\text{Al} + \text{Fe} \geq 1.5$  correspond to predominantly dioctahedral smectite. The large octahedral cation content (horizontal dashed line = 2.1) indicates a contribution from a trioctahedral component. The analysis with Mg 3.12 corresponds to talc.

between 1.5 and 2 per  $\text{O}_{10}(\text{OH})_2$ , but with a total octahedral (sum cations) content  $>2.1$  in many cases, with a maximum of 2.51 (Figure 8, Table 5). Such octahedral occupancy values indicate the presence of both dioctahedral and trioctahedral smectite. Those analyses with the greatest octahedral content ( $>2.47$  per  $\text{O}_{10}(\text{OH})_2$ ) and some others (8-S1, 9-S1, 10-S1, all three from different areas of a same large particle in sample 294) have Mg as the most abundant octahedral cation and have been labeled nontronite-saponite (Table 5) to indicate that the composition is approximately intermediate between the two. The datapoint with octahedral occupancy above 3 corresponds to talc (sample 292, 19-J in Table 5).

Other analyses (Table 5) have been labeled loosely as Fe-montmorillonite ( $1.4 > \text{Al} \geq 1$  and  $\text{Al} > \text{Fe} > 0.5$ ) and nontronite ( $\text{Fe} \geq 1$ ). These classifications were not intended to follow accepted definitions but simply to designate the present analyses according to their octahedral Fe content. The only analysis with  $\text{Al} \geq 1.4$  was the mica grain and, hence, no Al-montmorillonite grains were detected. Analyses 23-J, 12-S1, and 19-S1 (Table 5) were special cases in which no clear major component (Fe-montmorillonite, nontronite, or saponite) was observed; these were labeled Fe-Al-Mg and Mg-Fe-Al to indicate the order of octahedral cation content. The two analyses of Fe-Al-Mg were mainly dioctahedral and Mg-Fe-Al was of intermediate composition between di- and trioctahedral. Other analyses indicated a composition intermediate between nontronite and saponite (labeled Nont-sap in Table 5). Approximately half of the analyses reported no Mn.

This metal was  $>0.1$  per  $\text{O}_{10}(\text{OH})_2$  in only two of the analyses (0.25 for 11-J in sample 293; 0.11 for 3-S1 in 294), both corresponding to a nontronite (labeled nontronite (Mn) in Table 5). The other results found Mn values between 0.02 and 0.09 per  $\text{O}_{10}(\text{OH})_2$ .

Some of the SAED patterns with sharper and regular rings were used to measure  $d$  values, in an effort to identify the nature (Fe-montmorillonite, nontronite, saponite) of the particles or the possible presence of smectite crystals of different nature within the investigated area. Four such particles were analyzed. Smectite diffraction maxima were identified but the positions were not sufficiently constrained to differentiate between di- and trioctahedral smectite, and the position of some maxima appeared to be displaced. Thus, these measurements were not useful for further investigation of the nature of the smectite or proto-smectite in the samples.

## DISCUSSION

### Smectite crystallinity

The low crystallinity of the smectite particles is apparent in the XRD and SAED patterns. Despite the fact that this material appears to be abundant, as indicated by the SEM-EDX and TEM-AEM studies, the intensity of the diffraction peaks was very low (Figure 2, Table 1), as was the resolution of the SAED patterns of individual grains (Figure 6, Table 3). The IR spectra of the samples also showed rather broad, low-intensity features corresponding to smectite, compatible with low crystallinity materials (Figure 4). In the IR spectra, the smectite features were blurred by the mixture with Fe/MnOOH, also of low crystallinity. However, IR spectroscopy probes mineral volumes much smaller than XRD and the poorly defined smectite features in the IR spectra supports a lack of crystalline order even in the short-range distance. The chemical composition and the measurements in TEM images with lattice fringes indicated a fully formed smectite. However, (1) chemical irregularities may exist in the anionic content of the smectite or proto-smectite grains, undetectable with AEM, which result in inaccurate cation contents; and (2) the range of fringe width of 10–15 Å measured in the lattice-fringe images may be due not only to differential layer hydration, as in well crystallized smectite, but also to imperfect crystallization. Thus, according to the present data, this smectite displays characteristics of the fully formed mineral, such as the sheet, veil-like, and even lath habits; other characteristics, such as composition and the 10–15 Å layers typically found in lattice-fringe images of smectite, may or may not correspond, at least in some parts, to such a fully formed mineral. Finally, the crystal structure is so defective that diffraction patterns of both individual particles (SAED) and macroscopic volumes (XRD) are very imperfect. Such characteristics suggest



smectite in the process of crystallization, where the crystal-chemical-morphological modifications occur in a sequence of events that was not completed.

### Smectite composition

The smectite or proto-smectite particles are mainly of a dioctahedral nature, although most contain a trioctahedral component (Figure 8). Assuming that most of the Al and Fe is present in the dioctahedral phase (and thus that the trioctahedral phase is dominated by Mg), smectite particle composition can be further investigated by comparing their octahedral Fe and Al contents (Figure 9), which reveals that most particles have a nontronitic nature (trapezoid with the Al range 0–1 in Figure 9). A few others can be labeled as Fe-montmorillonites (Al range 1–1.4 in Figure 9). Iron, therefore, is an abundant component in all the particles analyzed. The relation between the di- and trioctahedral components cannot be deduced from the present data: topotactic growth or a more intimate structural relationship, from mixed-layering to domains within layers, may be the case. The multiple grains that were typically observed making up smectite particles (Figure 6) provide ample possibility for the aggregation of smectite grains of different compositions.

The occurrence of smectite within the series saponite, Fe-saponite, Mg-nontronite, and nontronite is frequent in relation to submarine hydrothermal fields. Cole (1988) described nontronite (octahedral content 1.91 atoms per  $\text{O}_{10}[\text{OH}]_2$ ), Mg-containing nontronite with octahedral occupancy intermediate between di- and trioctahedral

(2.34–2.56), and Fe-saponite (octahedral content 2.83–3.02) from the Atlantis II Deep, Red Sea. Cole and Shaw (1983) reviewed cases of authigenic submarine smectite and mentioned hydrothermal Mg-bearing nontronites placed near the discharge area with a typical octahedral occupancy of 2.34 atoms. Setti *et al.* (2004) provided compositions for Mg-Fe smectites formed by hydrothermal alteration of basalt with 2.5–2.6 octahedral atoms, sampled from a Cenozoic sequence in the Ross Sea, Antarctica. In other cases, however, no clear indication of compositions intermediate between nontronite and saponite were reported. Dymond and Eklund (1978) found Mg-rich nontronite with an octahedral content of 2.16, in a metalliferous sediment in Atlantis II, in the Bauer Basin, southeast Pacific. Cole (1985) described a Mg-rich nontronite with 2.11 atoms in the octahedral sheet, from the Bauer Deep, southeast Pacific. Severmann *et al.* (2004) found Mg-containing nontronite with a total octahedral composition of 2.0–2.13 in the Trans-Atlantic Geotraverse hydrothermal field, Mid-Atlantic Ridge. Singer *et al.* (1984) reported Mg-rich nontronite with octahedral occupancy of 1.88–2.08 in a core from the Tahiti–East Pacific Rise–New Zealand transect. Similarly, Murnane and Clague (1983) described Mg-containing nontronite with octahedral content of 2.02 from a sample from the Juan de Fuca Ridge. Accordingly, smectite with intermediate nontronite-saponite composition is frequent in submarine hydrothermal settings, although not the norm. In some cases, divalent cations such as Zn, Cu, and Mn are present in significant amounts.

No indication was given in the studies above as to whether the smectites with intermediate nontronite-saponite composition were a single phase or a mixture. Schwertmann *et al.* (1998) studied smectite and Fe oxides from the Atlantis II Deep in the Red Sea. The XRD patterns of the 060 peak contained two distinct peaks corresponding to di- and trioctahedral phases, and their chemistry also indicated Fe- and Mg-rich smectite with variable proportions of both metals. The results were compatible with two separate phases and with a single phase where the tri- and dioctahedral domains were sufficiently large to produce coherent XRD patterns independently. Schwertmann *et al.* (1998) did observe, however, that some of the chemical treatments used to remove Fe oxides affected the trioctahedral phase and not the dioctahedral one, which suggests their existence as independent phases as more likely.

Half of the smectite particles analyzed chemically in the present study contained Mn, in the range 0.02–0.25 atoms per  $\text{O}_{10}(\text{OH})_2$ , with an average of 0.06 (Table 5). The Mn is not considered to be due to contamination from Mn-rich oxyhydroxides, based on the good charge balance in the calculated structural formulae. Some reports of Mn concentrations in smectite from submarine hydrothermal fields and hydrothermally derived metalli-

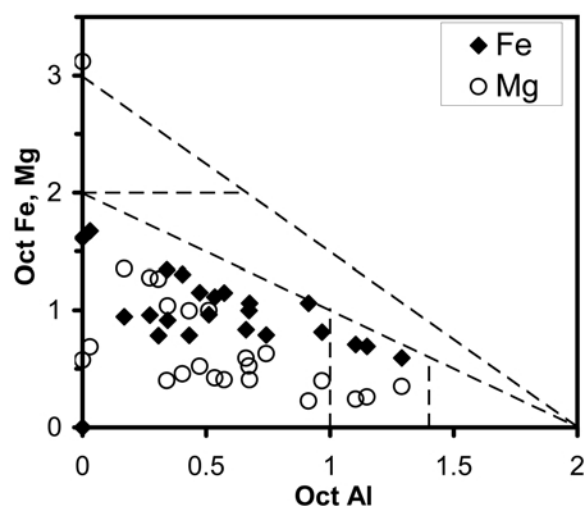


Figure 9. Plot of octahedral Al vs. octahedral Fe and Mg (per  $\text{O}_{10}[\text{OH}]_2$ ), from AEM analyses. The fields are marked according to Al, Fe, and Mg content. The analysis with Mg 3.12 corresponds to a particle of talc. The approximately linear progression of Fe from ~0.6 to ~1.7 indicates a mainly dioctahedral component in these analyses. The five Fe values which depart from this linear progression (with  $\text{Fe} < 1$ ,  $\text{Al} < 0.5$ ) correspond to analyses with a larger trioctahedral component.

ferous sediments range between 0.006 and 0.09 atoms per  $\text{O}_{10}(\text{OH})_2$  (Murnane and Clague, 1983; Cole and Shaw, 1983; Cole, 1985).

#### *Origin of smectite*

In principle, the (proto-)smectite in this study may have originated in three settings. One is within the hydrothermally active field, where hot fluids (up to  $\sim 100^\circ\text{C}$  for nontronite and saponite) would alter the basalt. Smectite particles newly formed beneath the seafloor should have detached from the rock and traveled with the hydrothermal plume to be deposited later with the Fe/MnOOH phases in the metalliferous sediments, away from the active hydrothermal field (Figure 1). In such a setting, however, the discharge of hydrothermal fluids is diffuse, through the basalt, and unable to detach and carry the clay particles away, and disconnected from the focused discharges that generate the hydrothermal plume.

The second setting is a chimney or hydrothermal vent where focused hydrothermal discharge is produced. 'Black smokers' or discharge points of high-temperature fluids cannot be such a setting because their typical temperatures of  $300\text{--}350^\circ\text{C}$  (Köhler *et al.*, 1994) favor the formation of beidellite, talc, and talc-smectite (or kerolite-smectite) rather than nontronite or saponite (Cole, 1983; Dekov *et al.*, 2008). 'White smokers,' however, with fluids in the range  $<100\text{--}300^\circ\text{C}$  may produce nontronite, which has been reported to form in the internal and external walls of the chimneys (Köhler *et al.*, 1994). The flow velocities of the fluids is of the order of  $\text{cm s}^{-1}$  (e.g. Von Damm, 1990), much slower than the  $\text{m s}^{-1}$  flow velocities in black smokers. The cooler temperature and slower flow velocity give white-smoker fluids less buoyancy and fewer opportunities to travel far from the vent point. The talc particle that was observed and analyzed with TEM-AEM (Table 5, sample 292, 19-J) probably formed at a focused discharge point and traveled with the hydrothermal plume.

The third possible setting where smectite originated is the metalliferous sediment itself, where smectite would form as a result of reactions between mineral phases and seawater at ambient temperature ( $\sim 4^\circ\text{C}$ ). In the metalliferous sediment, nontronite can form by the reaction between the low-crystallinity FeOOH phases, detrital silicates, and biogenic silica, the setting described by Cole (1985) and Chamley (1989). The samples in this study contained such detrital phases (Figure 2, Table 1) that could supply Si and Al to the newly formed (or forming) smectite. The few grains of a silica phase with signs of dissolution observed (e.g. Figure 3d) are perhaps an illustration of this process of Si contribution for smectite formation. In addition, silica of hydrothermal origin may be present in the metalliferous sediment. The hydrothermal fluids are Si-rich and, as the temperature of the fluids decreases in the hydrothermal plume, the reduction in silica solubility

may cause dissolved silica to polymerize and adsorb on the surface of Fe/MnOOH particles. In fact, silica polymers have a negative surface charge and they flocculate in the presence of metal hydroxyl complexes, which are positively charged (Williams and Crerar, 1985). Colloidal goethite surfaces are positively charged at approximately neutral pH values (point of zero charge at  $\sim 9$ ; Gaboriaud and Ehrhardt, 2003). Silicate anions adsorb to goethite, with a maximum adsorption at pH 7–9 in 0.1 M NaCl (Taylor, 1987). Thus, silica polymers are likely to coprecipitate with Fe/MnOOH phases in the cooling hydrothermal plume and become a reactive source of Si.

The chemistry of the smectite in the present study does not suggest a hydrothermal origin at the venting point because nontronite of such origin typically has very small Al concentrations (Murnane and Clague, 1983; Köhler *et al.*, 1994; Severmann *et al.*, 2004), whereas such concentration is significant in the studied samples (Table 5), pointing to formation reactions involving detrital phases. The significant Mn concentration found in half of the smectite samples suggests a Mn-rich formation environment, such as the metalliferous sediments in this study, where the MnO content varies between 6 and 12 wt.% (Table 2). The MnO content of fresh basalt samples in the area studied is 0.12 wt.%, indicating that this is a less likely formation setting. The Mn-based argument is far from conclusive, however, given the range of Mn concentrations found in the smectite samples in this study and in other smectites generated in immediate contact with hydrothermal fluids (e.g. Severmann *et al.*, 2004).

The crystallinity of the smectite is another factor with a possible bearing on its origin. Hot fluids are likely to accelerate reactions and produce a crystalline product faster than water at ambient ocean temperature. Smectite with an isotopic signature indicating formation by the action of hydrothermal fluids would appear as more crystalline. However, if smectite formation is mediated by low-crystallinity phases, and, in some cases, these phases ceased to be affected by hydrothermal fluids soon after their formation (e.g. by transport of the particles or cessation of hydrothermal activity), then such phases would bear a hydrothermal signature but evolve slowly toward a well crystallized smectite. Such smectitic phases would blur a trend of positive correlation between temperature and crystallinity. Well crystallized smectite, with temperatures of  $22^\circ\text{C}$  (Singer *et al.*, 1984),  $22\text{--}67^\circ\text{C}$  (Köhler *et al.*, 1994),  $54\text{--}96^\circ\text{C}$  (Severmann *et al.*, 2004),  $57^\circ\text{C}$  (Murnane and Clague, 1983); poorly to well crystallized smectite at  $30\text{--}50^\circ\text{C}$  (McMurtry and Yeh, 1981); and very well crystallized smectite with unknown formation temperature (Setti *et al.*, 2004) have been reported as originating at hydrothermal fields. Smectites reported as originating at ocean-bottom temperature have low (Masuda, 1995) or low to high crystallinity (Cole, 1985). The case reported by Masuda

(1995) is ambiguous with respect to temperature. He described nontronite covering Mn-rich Fe-Si oxides along a venting ridge. The water temperature at the venting point was 6°C, and 20–50°C at a depth of 50 cm below the surface of the sediment. Masuda (1995) suggested that the Fe-Si oxides precipitated immediately as the hydrothermal fluids mixed with seawater and the precipitate generated nontronite by dissolution-precipitation “at temperature higher than that of ambient seawater.” The inference is that nontronite formed between 6 and 3°C, the temperature of the venting fluids and bottom seawater, respectively. Such differentiation is scarcely meaningful. Masuda (1995) presumably implied that the fluids deeper in the sediment exerted a thermal influence, although this is not stated explicitly or supported with any argument. This nontronite is of interest because it contains an average of 0.065 Mn atoms per  $\text{O}_{10}(\text{OH})_{20}$ , a value well within the range of the samples in the present study. In Masuda’s (1995) study, nontronite originated in the metalliferous sediment, rather than in the vent source, although the two were in the same immediate vicinity.

To summarize, one can conclude that, considered together, the arguments presented above suggest that the formation of smectite in this study took place within the metalliferous sediment rather than by reactions involving hydrothermal fluids. The arguments are: (1) the large distance of the metalliferous sediments from the ocean ridge (and thus from possible hydrothermal sources); (2) the relatively high Al and significant Mn contents in smectite; and (3) the low crystallinity of the smectite. Iron was contributed by the Fe/MnOOH phases, Si by detrital silicates and amorphous silica of hydrothermal origin coprecipitated with Fe/MnOOH, and Mg by seawater. The reaction of formation/maturation was slow and the samples were in a stage of progressive crystallization, although apparently complete in terms of their chemistry.

#### Octahedral Fe-Mg composition

Whether the Mg- and Fe-rich components of the smectite are one or two phases is impossible to discern. Even if they are two phases, they are best explained as forming together in the metalliferous sediment, due to their intimate mixture down to microscopic scale. The possibility of an alternative origin was tested by plotting Mn concentrations in smectite vs. those of Fe and Mg, considering that if Mg-rich smectite had its origin away from the metalliferous sediments (e.g. at the basalt on the hydrothermal fields) Mn would appear to correlate positively with Fe and negatively with Mg. No correlation was apparent (Figure 10), suggesting no distinction in the formation environment.

Zierenberg and Shanks (1983, 1988) and Cole (1983, 1988) investigated the Fe-Mg composition of smectite samples from the Atlantis II Deep, Red Sea, and related them to O isotope compositions; positive correlations

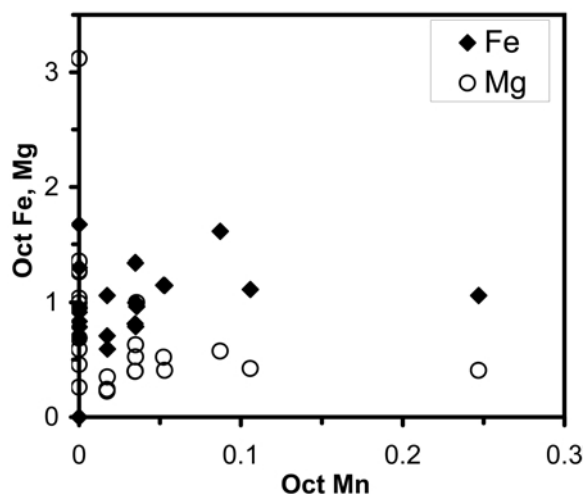


Figure 10. Octahedral Mn vs. octahedral Fe and Mg per  $\text{O}_{10}(\text{OH})_2$  for phyllosilicate particles. Data from AEM analyses. The datapoint with Mg > 3 corresponds to talc.

were obtained between the formation temperature and Mg content (Zierenberg and Shanks, 1988; Cole, 1988). This trend was further investigated in the present study using chemistry and temperature data from other locations. The result was that the data from the other locations have the opposite trend to those of Zierenberg and Shanks (1988) and Cole (1988), i.e. a negative correlation exists between the Mg content and the formation temperature derived from O isotope analyses (Figure 11). Interestingly, the minimum temperature in

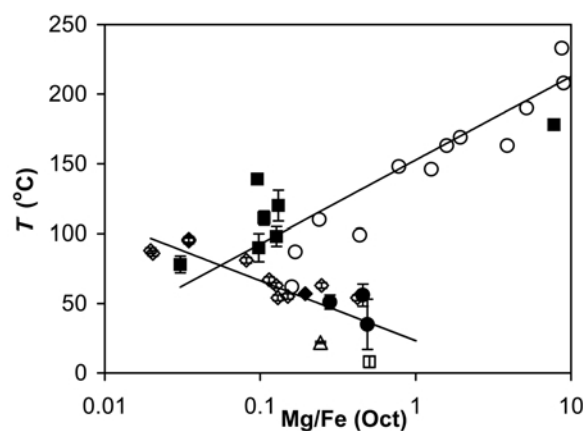


Figure 11. Octahedral Mg/Fe ratio vs. formation temperature from O isotope analysis, from the literature. Two opposing trends were obtained. Open circles: Zierenberg and Shanks (1983, 1988; no systematic error bars were provided by the authors), Atlantis II Deep, Red Sea; filled squares: Cole (1983, 1988), Atlantis II Deep; open diamonds: Severmann *et al.* (2004), Trans-Atlantic Geotraverse, Mid-Atlantic Ridge; open triangle: Singer *et al.* (1984), southwestern Pacific Basin; filled circles: McMurtry and Yeh (1981), Bauer Basin, East Pacific Rise; open square: Cole (1985), Bauer Deep; filled diamond: Murnane and Clague (1983), Juan de Fuca Ridge.

the sample series of Zierenberg and Shanks (1988) and Cole (1988) was approximately the maximum temperature in the series from the other authors, except for one sample (lowest open circle, Figure 11) of Zierenberg and Shanks (1988), suggesting that they corresponded to two different 'mineral' series (the word 'series' is used in a broad sense in this case). The samples with a negative Mg-temperature correlation were all clearly within the temperature range of smectite and the authors reported XRD patterns of their samples that correspond to smectite, and thus they were within the nontronite-saponite series. In the data with positive Mg-temperature correlation, however, the temperatures reached values above the usual smectite range and Cole (1988) indicated that (1) the Mg-Fe 2:1 clay series appeared to have nontronite and talc as end members, and (2) Mg-Fe smectite and kerolite (disordered talc) formed simultaneously. Similarly, some samples from Zierenberg and Shanks (1988) were from talc veins. Accordingly, the series in the Cole (1988) and Zierenberg and Shanks (1988) studies from the Atlantis II Deep would correspond to: smectite (in this case nontronite), talc-smectite (or kerolite-smectite), disordered talc (or kerolite), and talc. Such mineral series correspond to an increasing Mg content and temperature. Unfortunately, no XRD patterns were given in the studies by Zierenberg and Shanks (1983, 1988) and Cole (1983, 1988) to check this possibility. Their chemical data produced structural formulae with a wide range of interlayer charge, which would be compatible with a talc-smectite series (Zierenberg and Shanks, 1983; Cole, 1988). For a true nontronite-saponite series, therefore, from hydrothermal submarine fields and metalliferous sediments, Mg is broadly more abundant in smectite formed in the sediment without contact with hydrothermal fluids. Perhaps this greater Mg content is caused by incorporation from the ambient seawater in a slow maturation reaction.

#### *Mechanism of smectite formation*

Taitel-Goldman *et al.* (1999) and Taitel-Goldman and Singer (2002) described poorly ordered, metastable Si-Fe phases from the Atlantis II Deep sediments, with variable Si/Fe ratios. The phases were apparently precipitated at ~40°C in one of the layers of the stratified brine layers (with variable temperature, chemistry, pH, and Eh conditions) produced by the hydrothermal discharge, as indicated by the study of the Atlantis II Deep sediments and the successful synthesis of similar materials (Taitel-Goldman and Singer, 2002). The phases are then assumed to have formed quickly; were metastable, and transformed into both Fe oxides and nontronite, based on TEM-AEM and SAED analysis of individual particles. This transformation was slow, however, as the Si-Fe phases subsist in the sediment for thousands of years (Taitel-Goldman and Singer, 2002). The transformation into Fe oxides and nontronite

appears to be controlled (at least partially) by the Si-Fe ratio in the particles and the near environment, which change as Fe oxides or nontronite crystallize.

The Si-Fe phases could correspond to FeOOH with adsorbed silica as suggested above, or be the result of their reaction after adsorption. In any case, the existence of Si of hydrothermal origin in intimate contact with FeOOH precipitates from the hydrothermal fluids was demonstrated, and this is a potential source of Si in diagenetic reactions within the sediments. The Si-Fe phases and their slow reaction toward Fe oxides and nontronite fit well the formation model favored for the samples in the present study. Fe/MnOOH particles analyzed in this work always contained Al and Mg as well as Si, indicating that the original Si-Fe-MnOOH phases reacted completely and produced Fe/Mn oxides and oxyhydroxides and (proto-)smectite, some of which smectite was always present in Fe/MnOOH particles. As discussed above, the presence of Al and Mg is interpreted to indicate a contribution by detrital silicates and seawater, respectively. Taitel-Goldman and Singer (2001) described Mg-rich nontronites containing Al, also from the Atlantis II Deep, with octahedral occupancy of 2.13–2.31 per  $\text{O}_{10}(\text{OH})_2$ , and interpreted them as detrital, but the similarity with the samples in the present and other studies discussed above suggests that they are authigenic smectite formed in metalliferous sediments in contact with seawater rather than hydrothermal fluids.

The incorporation of Mn into smectite would also take place during the slow process of maturation. Most of the Mn in the present samples is  $\text{Mn}^{4+}$ , as indicated by the  $\delta\text{-MnO}_2$  phase (Figure 2, Table 1). The Mn in smectite is thought to be  $\text{Mn}^{2+}$ , as usually assumed. Manganese in the sediment probably does not experience reduction that would allow incorporation of Mn into the crystallizing smectite. Manganese oxide phases, however, are a mixture of  $\text{Mn}^{4+}$  and  $\text{Mn}^{2+}$ , where better crystallized phases like birnessite and todorokite have a larger proportion of  $\text{Mn}^{4+}$ . Buatier *et al.* (2004) found an average valence of 3.7 in the above phases and 2–2.3 in amorphous MnOOH phases from the Juan de Fuca Ridge. Such amorphous phases may have contributed the  $\text{Mn}^{2+}$  present in smectite.

#### SUMMARY

The metalliferous sediments returned by the *HMS Challenger* expedition (1872–1876) from the ocean floor off the Chilean coast contain a proto-smectitic material characterized by low crystallinity but chemical and morphological features corresponding to mature smectite. This proto-smectite is like a dioctahedral nontronite, but contains a large proportion of a trioctahedral (Mg-rich) component. The di- and trioctahedral components are mixed down to the microscopic scale, but whether they are one individual



or two separate phases could not be discerned. Manganese is a significant component in the material (range 0.02–0.25, average 0.06 atoms per  $\text{O}_{10}[\text{OH}]_2$ ). The most likely origin of the proto-smectite is the slow reaction (thousands of years?) of  $\text{Fe/MnOOH}$  phases with seawater (contributing Mg), detrital mineral phases (contributing Al and Si), and amorphous Si of hydrothermal origin adsorbed on  $\text{Fe/MnOOH}$  in the metalliferous sediment, away from the hydrothermal fluid sources and thus at low temperature.

#### ACKNOWLEDGMENTS

The authors thank M.M. Abad for technical support with the TEM-AEM analysis, B. Lanson for providing information about the nature of the  $\delta\text{-MnO}_2$  phase, and N. Taitel-Goldman for very helpful advice and discussion at an early stage of the study. They also thank three anonymous reviewers for their helpful comments. This work was partly funded by the 'Synthesis' program of the European Community and Research Project no. CGL2007-66744-C02-01/BTE of the Spanish MICINN.

#### REFERENCES

- Boström, K. (1973) The origin and fate of ferromanganous active ridge sediments. *Stockholm Contributions in Geology*, **27**, 149–243.
- Brown, G. (1980) Associated minerals. Pp. 361–410 in: *Crystal Structure of Clay Minerals and Their X-ray Identification* (G.W. Brindley and G. Brown, editors). Monograph 5, Mineralogical Society, London.
- Buatier, M.D., Guillaume, D., Wheat, C.G., Hervé, L., and Adatte, T. (2004) Mineralogical characterization and genesis of hydrothermal Mn oxides from the flank of the Juan de Fuca Ridge. *American Mineralogist*, **89**, 1807–1815.
- Chamley, H. (1989) Metalliferous clay in deep sea. Pp. 259–290 in: *Clay Sedimentology*. Springer-Verlag, Berlin.
- Cliff, G. and Lorimer, G.W. (1975) The quantitative analysis of thin specimens. *Journal of Microscopy*, **103**, 203–207.
- Cole, T.G. (1983) Oxygen isotope geothermometry and origin of smectites in the Atlantis II Deep, Red Sea. *Earth and Planetary Science Letters*, **66**, 166–176.
- Cole, T.G. (1985) Composition, oxygen isotope geochemistry and origin of smectite in the metalliferous sediments of the Bauer Deep, southeast Pacific. *Geochimica et Cosmochimica Acta*, **49**, 221–235.
- Cole, T.G. (1988) The nature and origin of smectite in the Atlantis II Deep, Red Sea. *The Canadian Mineralogist*, **26**, 755–763.
- Cole, T.G. and Shaw, H.F. (1983) The nature and origin of authigenic smectites in some recent marine sediments. *Clay Minerals*, **18**, 239–252.
- Dekov, V.M., Kamenov, G.D., Stummeyer, J., Thiry, M., Savelli, C., Shanks, W.C., Fortin, D., Kuzmann, E., and Vertes, A. (2007) Hydrothermal nontronite formation at Eolo Seamount (Aeolian volcanic arc, Tyrrhenian Sea). *Chemical Geology*, **245**, 103–119.
- Dekov, V.M., Cuadros, J., Shanks, W., and Koski, R.A. (2008) Deposition of talc-kerolite-smectite-smectite at seafloor hydrothermal vent fields: Evidence from mineralogical, geochemical and oxygen isotope studies. *Chemical Geology*, **247**, 171–194.
- Dekov, V.M., Cuadros, J., Kamenov, G.D., Weiss, D., Arnold, T., Basak, C., and Rochette, P. (2010) Metalliferous sediments from the H.M.S. Challenger voyage (1872–1876). *Geochimica et Cosmochimica Acta*, **74**, 5019–5038.
- Dymond, J. and Eklund, W. (1978) A microprobe study of metalliferous sediment components. *Earth and Planetary Science Letters*, **40**, 243–251.
- Froelich, P.N., Bender, M.L., and Heath, G.R. (1977) Phosphorous accumulation rates in metalliferous sediments on the East Pacific Rise. *Earth and Planetary Science Letters*, **34**, 351–359.
- Gaboriaud, F. and Ehrhardt, J. (2003) Effects of different crystal faces on the surface charge of colloidal goethite ( $\alpha\text{-FeOOH}$ ) particles: An experimental and modeling study. *Geochimica et Cosmochimica Acta*, **67**, 967–983.
- Gurvich, E.G. (2006) *Metalliferous Sediments of World Ocean. Fundamental Theory of Deep-Sea Hydrothermal Sedimentation*. Springer, Heidelberg, Germany, 420 pp.
- Heath, G.R. and Dymond, J. (1977) Genesis and transformation of metalliferous sediments from the East Pacific Rise, Bauer Deep, and Central Basin, northwest Nazca plate. *Geological Society of America Bulletin*, **88**, 723–733.
- Huertas, F.J., Cuadros, J., Huertas, F., and Linares, J. (2000) Experimental study of the hydrothermal formation of smectite in the beidellite-saponite series. *American Journal of Science*, **300**, 504–527.
- Huertas, F.J., Fiore, S., and Linares, J. (2004) In situ transformation of amorphous gels into spherical aggregates of kaolinite: An HRTEM study. *Clay Minerals*, **39**, 421–431.
- Jürgensen, A., Widmeyer, J.R., Gordon, R., Bendell-Young, L.I., Moore, M.M., and Crozier, E.D. (2004) The structure of the manganese oxide on the sheath of the bacterium *Leptothrix discophora*: An XAFS study. *American Mineralogist*, **89**, 1110–1118.
- Köhler, B., Singer, A., and Stoffers, P. (1994) Biogenic nontronite from marine white smoker chimneys. *Clays and Clay Minerals*, **42**, 689–701.
- Lonsdale, P. (1976) Abyssal circulation of the southeastern Pacific and some geological implications. *Journal of Geophysical Research*, **81**, 1163–1176.
- Mariénfeld, P. and Marchig, V. (1992) Indications of hydrothermal activity at the Chile Ridge spreading centre. *Marine Geology*, **105**, 241–252.
- Masuda, H. (1995) Iron-rich smectite formation in the hydrothermal sediment of Iheya Basin, Okinawa Trough. Pp. 509–521 in: *Biogeochemical Processes and Ocean Flux in the Western Pacific* (H. Sakai and Y. Nozaki, editors). Terra Scientific Publishing Company, Tokyo.
- Mazer, J.J., Bates, J.K., Bradley, J.P., Bradley, C.R., and Stevenson, C.M. (1992) Alteration of tectites to form weathering products. *Nature*, **357**, 573–576.
- McMurtry, G.M. and Yeh, H.W. (1981) Hydrothermal clay mineral formation of East Pacific rise and Bauer basin sediments. *Chemical Geology*, **32**, 189–205.
- Müller, G. and Förstner, U. (1976) Primary nontronite from the Venezuelan Guyana: additional primary occurrences (Red Sea, Lake Malawi). *American Mineralogist*, **61**, 500–501.
- Murnane, R. and Clague, D.A. (1983) Nontronite from a low-temperature hydrothermal system on the Juan de Fuca Ridge. *Earth and Planetary Science Letters*, **65**, 343–352.
- Murray, J. and Renard, A.F. (1891) *Report on deep-sea deposits based on the specimens collected during the voyage of H.M.S. Challenger in the years 1872–1876*. Neill and Company, Edinburgh, 525 pp.
- Newman, A.C.D. and Brown, G. (1987) The chemical constitution of clays. Pp. 1–128 in: *Chemistry of Clays and Clay Minerals* (A.C.D. Newman, editor). Mineralogical Society Monograph 6, London.
- Russell, J.D. and Fraser, R. (1994) Infrared methods. Pp. 11–67 in: *Clay Mineralogy: Spectroscopic and Chemical Determinative Methods* (M.J. Wilson, editor). Chapman &

- Hall, London.
- Schwertmann, U., Friedl, J., Stanjek, H., Murad, E., and Bender Koch, C. (1998) Iron oxides and smectites in sediments from the Atlantis II Deep, Red Sea. *European Journal of Mineralogy*, **10**, 953–967.
- Setti, M., Marinoni, L., and López-Galindo, A. (2004) Mineralogical and geochemical characteristics (major, minor, trace elements and REE) of detrital and authigenic clay minerals in a Cenozoic sequence from Ross Sea, Antarctica. *Clay Minerals*, **39**, 405–421.
- Severmann, S., Mills, R.A., Palmer, M.R., and Fallick, A.E. (2004) The origin of clay minerals in active and relict hydrothermal deposits. *Geochimica et Cosmochimica Acta*, **68**, 73–88.
- Singer, A., Stoffers, P., Heller-Kalai, L., and Szafrank, D. (1984) Nontronite in a deep-sea core from the South Pacific. *Clays and Clay Minerals*, **32**, 375–383.
- Stoffers, P., Lallier-Verges, E., Plüger, W., Schmitz, W., Bonnot-Courtois, C., and Hoffert, M. (1984) A “fossil” hydrothermal deposit in the South Pacific. *Marine Geology*, **62**, 133–151.
- Stoffers, P., Worthington, T., Hekinian, R., Petersen, S., Hannington, M., Türkay, M., Ackermann, D., Borowski, C., Dankert, S., Fretzdorff, S., Haase, K., Hoppe, A., Jonasson, I., Kuhn, T., Lancaster, R., Monecke, T., Renno, A., Stecher, J., and Weiershäuser, L. (2002) Widespread silicic volcanism and hydrothermal activity on the northern Pacific-Antarctic Ridge. *InterRidge News*, **11**, 30–32.
- Taitel-Goldman, N. and Singer, A. (2001) High-resolution transmission electron microscopy study of newly formed sediments in the Atlantis II Deep, Red Sea. *Clays and Clay Minerals*, **49**, 174–182.
- Taitel-Goldman, N. and Singer, A. (2002) Metastable Si-Fe phases in hydrothermal sediments of Atlantis II Deep, Red Sea. *Clay Minerals*, **37**, 235–248.
- Taitel-Goldman, N., Singer, A., and Stoffers, P. (1999) A new short-range ordered, Fe-Si phase in the Atlantis II Deep, Red Sea hydrothermal sediments. Pp. 697–705 in: *Clays for Our Future* (H. Kodama, A.R. Mermut and J.K. Torrance, editors). Proceedings of the 11<sup>th</sup> International Clay Conference, Ottawa, Canada, 1997. ICC97 Organizing Committee, Ottawa.
- Taylor, R.M. (1987) Non-silicate oxides and hydroxides. Pp. 129–201 in: *Chemistry of Clays and Clay Minerals* (A.C.D. Newman, editor). Mineralogical Society Monograph **6**, London.
- Tazaki, K., Fyfe, W.S., and van der Gaast, S.J. (1989) Growth of clay minerals in natural and synthetic glasses. *Clays and Clay Minerals*, **37**, 348–354.
- Thompson, M. and Walsh, J.N. (2003) *Handbook of Inductively Coupled Plasma Atomic Emission Spectrometry*. Viridian, Woking, Surrey, UK.
- Williams, L.A. and Crerar, D. (1985) Silica diagenesis, II. General mechanisms. *Journal of Sedimentary Petrology*, **55**, 312–321.
- Von Damm, K.L. (1990) Seafloor hydrothermal activity: Black smoker chemistry and chimneys. *Annual Review of Earth and Planetary Science*, **18**, 173–204.
- Zierenberg, R.A. and Shanks, W.C. III (1983) Mineralogy and geochemistry of epigenetic features in metalliferous sediment, Atlantis II Deep, Red Sea. *Economic Geology*, **78**, 57–72.
- Zierenberg, R.A. and Shanks, W.C. III (1988) Isotopic studies of epigenetic features in metalliferous sediment, Atlantis II Deep, Red Sea. *The Canadian Mineralogist*, **26**, 737–753.

(Received 28 September 2010; revised 26 April 2011; Ms. 488; A.E. R. Dohrmann)